

RSC Advances



This article can be cited before page numbers have been issued, to do this please use: R. Jiang, D. T. Tran and J. P. MacClure, *RSC Adv.*, 2016, DOI: 10.1039/C6RA15040C.



This is an *Accepted Manuscript*, which has been through the Royal Society of Chemistry peer review process and has been accepted for publication.

Accepted Manuscripts are published online shortly after acceptance, before technical editing, formatting and proof reading. Using this free service, authors can make their results available to the community, in citable form, before we publish the edited article. This *Accepted Manuscript* will be replaced by the edited, formatted and paginated article as soon as this is available.

You can find more information about *Accepted Manuscripts* in the [Information for Authors](#).

Please note that technical editing may introduce minor changes to the text and/or graphics, which may alter content. The journal's standard [Terms & Conditions](#) and the [Ethical guidelines](#) still apply. In no event shall the Royal Society of Chemistry be held responsible for any errors or omissions in this *Accepted Manuscript* or any consequences arising from the use of any information it contains.

Non-Precious Mn_{1.5}Co_{1.5}O₄-FeN_x/C Nanocomposite as A Synergistic Catalyst for Oxygen Reduction in Alkaline Media

Rongzhong Jiang*, Dat T. Tran, and Joshua P. McClure

Phone: 301-394-0295. Fax: 301-394-0273. Email: Rongzhong.jiang.civ@mail.mil

Sensors and Electron Devices Directorate, U.S. Army Research Laboratory, 2800 Powder Mill Road, Adelphi, MD 20783-1197, United States.

KEYWORDS: Nanocomposite material, ORR catalyst, Double synergistic effects, (Mn, Co)₃O₄, FeN_x/C

ABSTRACT: In this study we show a method of preparing a high performing catalyst by designing functional nano boundaries in a nanocomposite material. A non-precious nanocomposite material composed of spinel Mn_{1.5}Co_{1.5}O₄ nano crystals and FeN_x-functionalized graphene nano platelets (FeN_x/C) was synthesized by an ultrasonic process. The crystal structure and elemental composition of the bimetal oxide were determined by X-ray diffraction (XRD) and energy dispersive X-ray spectroscopy (EDS). The surface morphology of the Mn_{1.5}Co_{1.5}O₄-FeN_x/C nanocomposite was characterized with transmission electron microscopy (TEM) and scanning transmission electron microscopy (STEM). The catalytic activity for oxygen reduction reaction (ORR) was analyzed by electrochemical method. The enhancement of activity for the ORR at the nanocomposite material is attributed to double synergistic effects from the bimetal particles and the FeN_x/C nano sheets. The nanocomposite material is able to catalyze 4-electron oxygen reduction to generate water in alkaline media with high kinetic rate constant ($7.6 \times 10^{-2} \text{ cm} \cdot \text{s}^{-1}$ at 0.7V vs. reversible hydrogen electrode, RHE). Finally, the activity and stability of the nanocomposite material were compared with that of 40% Pt supported on active carbon (40% Pt/C), which reaches 95% activity and a comparable stability of 40% Pt/C at 0.7V (vs. RHE).

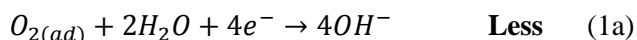
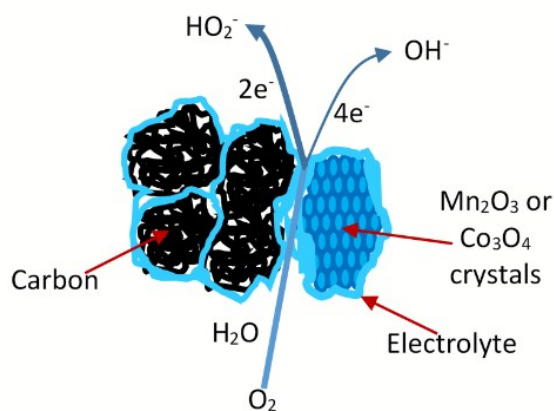
1.0 INTRODUCTION

Fuel cells are ideal energy conversion devices that efficiently use fuel with low to zero emission. However, the cost of fuel cell materials and components is unacceptably high for commercial application. For example, platinum catalysts are common core materials in fuel cell devices, which accounts for ~60% of the total cost of fuel cell stacks [1]. Non-precious materials as an alternative for fuel cell catalysts have received much attention. Unpyrolyzed and pyrolyzed transition metal macrocycles [2-10], as a large group of non-precious materials, were extensively investigated for catalytic oxygen reduction reaction (ORR). It is interesting that the macrocycles after pyrolysis contain only carbon with micro amount of nitrogen and metal atoms (~5%), but have better activity and stability than those that have not been pyrolyzed [9-10]. Therefore, major efforts have focused on pyrolyzed macrocycles such as nitrogen-doped carbons (N_x/C), as well as metal-nitrogen co-doped carbon (MN_x/C). Lately, it has been reported that the N_x/C or MN_x/C catalysts may be obtained from non-macrocylic precursors, such as nitrogen-rich polymers and bio-materials [11-20]. Although the N_x/C or MN_x/C materials have good initial activity, their activity decays rapidly with time, especially in acidic media. The gradual activity decrease is attributed to continuous loss of catalytic sites in acidic media and harsh fuel cell operating condition. The decrease in catalytic stability is potentially mitigated by increasing the concentration of catalytic sites in the MN_x/C materials [20]. In addition to N_x/C

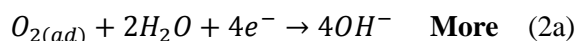
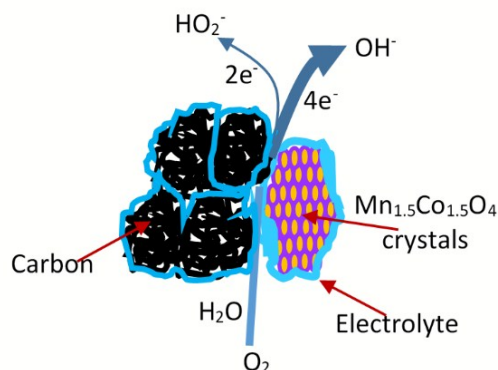
and MN_x/C catalysts, another notable group of non-precious materials investigated for the ORR are transition metal oxides [21-34], which show promising activity and persistent stability in alkaline media. Non-noble metal oxides are earthy-abundant, low cost, and ideal catalyst materials for fuel cells with alkaline electrolyte membranes or anion exchange membranes [35-38]. As non-noble metal oxides are poorly electrically conductive, they have to be supported on inert conductive materials such as high surface area carbons. However, the ORR mechanisms for metal oxides are complex. There are 2-electron, mix 2 & 4-electron, and 4-electron reactions, which often depend on the metal oxides' structure, composition, morphology, supporting materials, and dopants. The 2-electron reaction mainly occurs on free metal oxides, carbon supports, and their simple mixtures [21, 23, 25-26, 31-32, 34]. The 4-electron reaction mainly occurs on the nano-structures of metal oxides coupled with a functional support or a dopant, such as MnO_2 intercalated in graphene oxides [23], Co_3O_4 nano-rod supported on carbon [29], Co_3O_4 nanocrystals on graphene [30], Co_3O_4 nano-sheets interleaved with graphene sheets [33], and mesoporous Mn_2O_3 doped with Pd nanoparticles [32]. The mechanism of 4-electron reaction is attributed to a synergistic effect at the nano boundaries between metal atoms and the support. Most recently, more innovative nano materials were synthesized with high catalytic activity and stability. For example, Xia et al [39] synthesized a high performing bifunctional catalyst composed of hollow frameworks of nitrogen-doped carbon nanotubes for oxygen reduction and evolution.

In the present research, we attempt to explore how oxygen is reduced at the nano boundaries between metal oxides and carbon supports. Scheme 1 shows a mixed mechanism containing a 4-electron O_2 reduction reaction to produce water (Scheme 1a) and a 2-electron reaction to produce hydrogen peroxide (Scheme 1b) at the boundary between a mono-metal oxide (Mn_2O_3/C or Co_3O_4/C) and a traditional carbon support (un-doped).

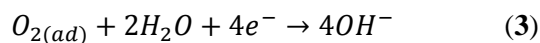
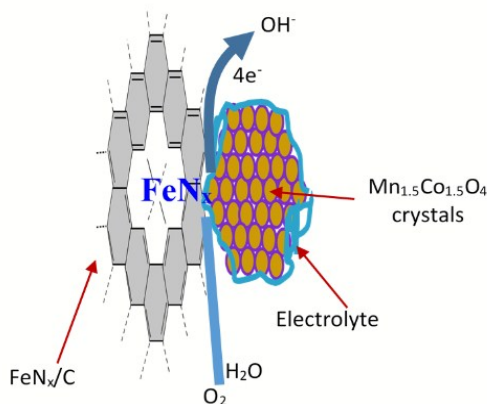
Scheme 1: Mixed mechanism for ORR at mono-metal oxide and un-doped carbon support



In order to minimize the 2-electron reduction of oxygen, we combined the two metals to form a bimetal oxide, and observed an enhancement of the ORR activity at the boundaries between the bimetal oxide, $Mn_{1.5}Co_{1.5}O_4$, and the carbon support. Scheme 2 shows a mixed mechanism of ORR with a larger fraction of the 4-electron reaction (Scheme 2a) compared to the smaller 2-electron reduction fraction (Scheme 2b).

Scheme 2: Mixed mechanism for ORR at bimetal oxide and un-doped carbon support

To further increase the catalytic activity, we used a functional carbon (i.e., a metal-nitrogen co-doped graphene) as a support to replace the traditional carbon. We prepared the nanocomposite material, $Mn_{1.5}Co_{1.5}O_4$, supported on FeN_x/C , by ultrasonic processing. Interestingly, we realized a near completed 4-electron oxygen reduction reaction for the nano-composite as a catalyst. Scheme 3 shows a 4-electron reaction mechanism of ORR at the nano boundaries between the bimetal sites and the FeN_x/C nano sheets.

Scheme 3: A mechanism for ORR at bimetal oxide and FeN_x -doped carbon support

The enhancement of catalytic activity is believed to be a synergistic effect of the bimetal atoms (Mn and Co), and a synergistic effect of the bimetal oxide nano crystals and the FeN_x/C nano sheets.

2.0 EXPERIMENTAL SECTION

2.1 Chemicals and Materials. Hemin from porcine, Cobalt (II) oxalate dihydrate ($\text{CoC}_2\text{O}_4 \cdot 2\text{H}_2\text{O}$), Manganese (II) oxalate dihydrate ($\text{MnC}_2\text{O}_4 \cdot 2\text{H}_2\text{O}$), and ammonium hydroxide (28% NH_3), were purchased from Aldrich. Graphene nano platelets (GNP) with a BET surface area between 600 – 650 m^2/g were purchased from Cheap Tubes Inc. Platinum nano catalyst supported on 60% active carbon (40% Pt/C) was purchased from Johnson Matthey. Deionized water was used for all synthesis and experiments.

2.2 Synthesis of Mn_2O_3 , Co_3O_4 and $\text{Mn}_{1.5}\text{Co}_{1.5}\text{O}_4$. 1g $\text{CoC}_2\text{O}_4 \cdot 2\text{H}_2\text{O}$ and 1g $\text{MnC}_2\text{O}_4 \cdot 2\text{H}_2\text{O}$ were mixed with 3 mL NH_4OH water, ground to a paste and dried at 70°C. The dry mixture was put in a ceramic boat and heat-treated at 400°C in the presence of air for two hours. A bimetal oxide with black color was obtained, and determined as $\text{Mn}_{1.5}\text{Co}_{1.5}\text{O}_4$. The Mn_2O_3 and Co_3O_4 were synthesized by weighing 2g $\text{MnC}_2\text{O}_4 \cdot 2\text{H}_2\text{O}$ and 2g $\text{CoC}_2\text{O}_4 \cdot 2\text{H}_2\text{O}$, respectively, and following the same procedure as that of making $\text{Mn}_{1.5}\text{Co}_{1.5}\text{O}_4$, except processing and heat-treating them separately. For comparison, a mixture of Mn_2O_3 and Co_3O_4 was also prepared by ultrasonic treatment of equal amount of Mn_2O_3 and Co_3O_4 in water for 30 minutes and dried at 60°C.

2.3 Synthesis of FeN_x/C . Synthesized according to our previous reports [6-8] and briefly described here. 1g hemin and 1g GNP were uniformly dispersed in 50 mL N, N- Dimethylformamide (DMF). After drying on a hot-plate, the mixture was placed in a ceramic boat and sent to a tubular furnace for heat-treatment for 2 hours under a nitrogen atmosphere at 600 °C. The material after pyrolysis contained 4.9% Fe (w/w), 4.3% N (w/w), 1.5% H (w/w) and 77.8% C(w/w), with N/Fe atomic ratio ~3.5 by elemental analysis.

2.4 Synthesis of $\text{Mn}_{1.5}\text{Co}_{1.5}\text{O}_4\text{-FeN}_x/\text{C}$ Nanocomposite. The nanocomposite was synthesized by ultrasonically processing $\text{Mn}_{1.5}\text{Co}_{1.5}\text{O}_4$ and FeN_x/C to break the large particles into nano-sized particles. A Branson Sonifier 450 was used with an ultrasound tip source. Here, 32 mg $\text{Mn}_{1.5}\text{Co}_{1.5}\text{O}_4$ and 75 mg FeN_x/C were mixed in a small beaker containing 4 mL 1-propanol and 4 mL water. The samples were cooled in an ice bath, and processed at a duty cycle of 40 and output control of 8 for 20 minutes. After ultrasound treatment an ink-like solution was obtained, containing 4 mg/mL $\text{Mn}_{1.5}\text{Co}_{1.5}\text{O}_4$ dry sample and 9.4 mg/mL FeN_x/C . The dried material is referred to a $\text{Mn}_{1.5}\text{Co}_{1.5}\text{O}_4\text{-FeN}_x/\text{C}$ nanocomposite. The ink was directly used for electrochemical analysis by adding 5% Nafion solution as binder. As mentioned in our previous report [6], the ultrasound method is a powerful tool for processing nano-materials. Moreover, the FeN_x/C is a high surface area nanomaterial with high electric conductivities and relatively good chemical stabilities to accommodate the metal oxides. The $\text{Mn}_2\text{O}_3/\text{C}$, $\text{Co}_3\text{O}_4/\text{C}$, and $\text{Mn}_{1.5}\text{Co}_{1.5}\text{O}_4/\text{C}$ samples were prepared by ultrasonically mixing with 70% GNP in chilled in an ice bath.

2.5 Instrumental Analysis. X-Ray Diffraction data (XRD) were obtained from a Rigaku Ultima III instrument with Cu $K\alpha$ radiation ($\lambda = 1.5418 \text{ \AA}$) using a Bragg-Brentano Configuration. The measurements were conducted with a scan rate of 1.0 degree (2θ) per minute; and each diffraction data point was collected at the interval of 0.02 degree (2θ) for the total spectrum range of 10 to 80 degree (2θ). Transmission electron microscopy (TEM) were obtained with a high-resolution JEOL 2100 FE instrument equipped with an EDAX X-ray detector and a high angle annular dark field (HAADF) detector. Before imaging, a solution was prepared by adding 5 mg of the catalyst into 5 mL of 1-propanol followed by a short ultrasonic bath (Branson 3510) treatment. An aliquot of ink was loaded onto a QUANTIFOIL®–Holey Carbon Films (0.6 μm hole, 1.6 μm space 300 mesh copper grid, Electron Microscopy Science) with a micro-pipette and dried overnight at room temperature. Elemental mapping were obtained by scanning transmission electron microscopy (STEM) based on atomic resolution HAADF imaging. Elemental analysis was obtained by energy dispersive X-ray spectroscopy (EDS).

2.6 Electrochemical Characterization. A Pine Bipotentiostat RDE4 was used for electrochemical characterization. A glassy carbon (GC) disk electrode (0.196 cm^2) and a ring-disk electrode were used. The ring-disk electrode had a GC disk electrode (0.247 cm^2) and a Pt-ring electrode (collection coefficient 0.37). A catalyst sample was first suspended in 1:1 water/1-propanol solution and cooled in an ice bath. The catalyst ink was prepared by ultrasonic treatment with a Branson Sonifier 450 with a duty cycle of 40 and an output control of 8 for 10 minutes. The final catalyst content was 4 mg/mL metal oxides ($\text{Mn}_{1.5}\text{Co}_{1.5}\text{O}_4$, or Mn_2O_3 , or Co_3O_4). Then, 10 μL of catalyst ink was coated on a GC disk working electrode for RDE experiments; and on the disk electrode of the ring-disk electrode for RRDE experiments, respectively. The ink was dried at 40°C for over 60 minutes. The final coating on the GC disk electrode contained 95% total catalyst materials and 5% dry Nafion with a metal oxide loading of $0.20 \text{ mg}\cdot\text{cm}^{-2}$. An ink of 40% Pt/C was prepared using the same procedure as that discussed for the metal oxide samples. The final loading of 40% Pt/C on the GC electrode was $0.20 \text{ mg}\cdot\text{cm}^{-2}$. The catalyst coated electrode was mounted onto a Pine ASR rotator and used as the working electrode. All voltammetry experiments were performed in argon (Ar.) or O_2 saturated 0.1M potassium hydroxide (KOH) solution at room temperature ($20 \pm 1^\circ\text{C}$). A three electrode glass cell was used for electrochemical study containing three compartments separated by porous ceramic layers. A platinum wire counter electrode and a saturated calomel reference electrode (SCE) were used in the cell. The experimental results were reported based on reversible hydrogen electrode (RHE). The difference between SCE and RHE was experimentally determined with an SCE and a fresh-prepared RHE in 0.1M KOH solution in the same electrochemical cell. The current density reported in this article is based on the geometrical area of the GC disk electrode ($\text{mA}\cdot\text{cm}^{-2}$), which can be changed to current density based on mass ($\text{mA}\cdot\text{mg}^{-1}$) by simply multiplying a factor of 5 according to the mass of the catalyst loading.

3.0 RESULTS AND DISCUSSION

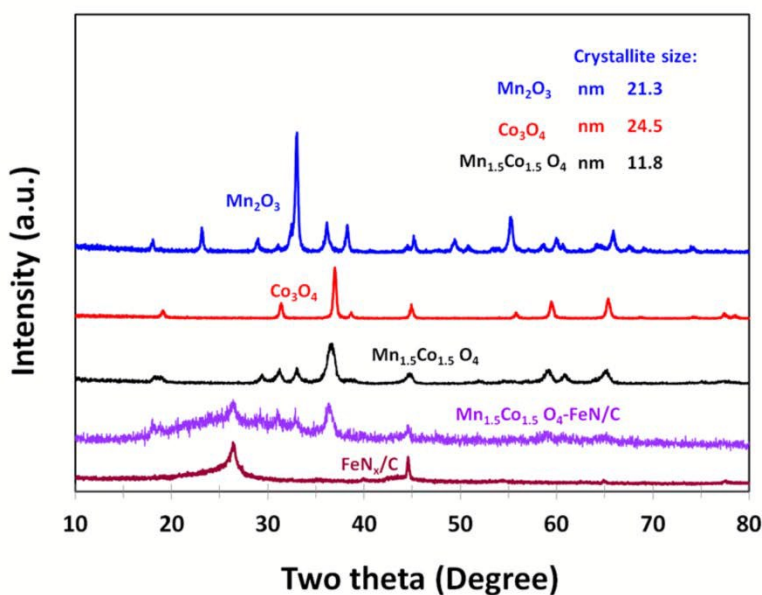


Fig. 1. X-ray diffraction pattern of non-precious metal oxides, FeN_x -doped carbon and $\text{Mn}_{1.5}\text{Co}_{1.5}\text{O}_4$ - FeN_x/C nanocomposite.

3.1 XRD Results. The composition and morphology of several metal oxides were characterized with XRD, including the mono metal oxides (manganese oxide and cobalt oxide) and the bimetal oxide (manganese-cobalt oxide). As shown in Figure 1, all of them are highly crystallized. Their structures and compositions were determined with the XRD results, as α - Mn_2O_3 , Co_3O_4 , and $(\text{Mn}, \text{Co})_3\text{O}_4$, respectively. The atomic ratio of Mn to Co in the $(\text{Mn}, \text{Co})_3\text{O}_4$ crystals was further determined with EDS analysis, as ~ 1 (see the following EDS results). Therefore, it is determined that the bimetal oxide is $\text{Mn}_{1.5}\text{Co}_{1.5}\text{O}_4$ with a spinel structure. The crystallite size of $\text{Mn}_{1.5}\text{Co}_{1.5}\text{O}_4$ (11.8 nm) is significantly smaller than that of α - Mn_2O_3 (21.3 nm) or Co_3O_4 (24.5 nm). As shown in Figure 1, the XRD pattern of the $\text{Mn}_{1.5}\text{Co}_{1.5}\text{O}_4$ - FeN_x/C nanocomposite has the main peaks of both $\text{Mn}_{1.5}\text{Co}_{1.5}\text{O}_4$ and FeN_x/C . The chemical states of Co and Mn in the nanocomposite have been cleared from the XRD results showing in Figure 1, as $\text{Co}^{3+}/\text{Co}^{2+}$ and $\text{Mn}^{3+}/\text{Mn}^{2+}$. The chemical state of nitrogen in the nanocomposite can be determined from X-ray photoelectron spectroscopy (XPS) according to the reports [13, 41]. For Fe-porphyrins pyrolyzed at 600 °C [41], the deconvoluted high-resolution XPS spectra at the N1s region showed three peaks, assigned as pyrrolic, pyridinic and Fe- N_4 based nitrogen atoms, with peak positions (binding energy, eV) at 400.3, 398.8 and 398.1, respectively. The chemical state of iron has been determined from the electrochemical results (cyclic voltammograms), as $\text{Fe}^{+3}/\text{Fe}^{+2}$.

3.2 TEM and STEM Images.

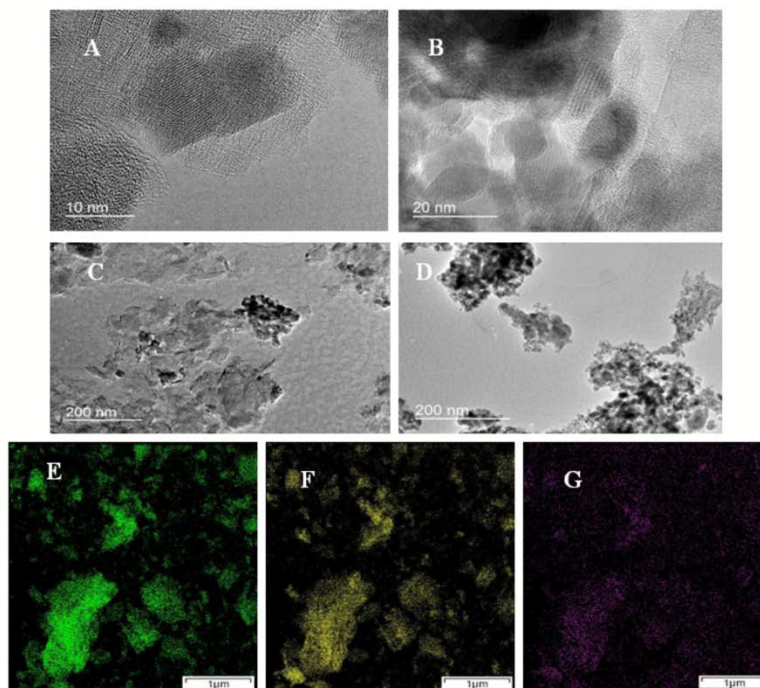


Fig.2. TEM images of $\text{Mn}_{1.5}\text{Co}_{1.5}\text{O}_4$ - FeN_x/C (A-C), and $\text{Mn}_{1.5}\text{Co}_{1.5}\text{O}_4$ (D); and elemental maps of $\text{Mn}_{1.5}\text{Co}_{1.5}\text{O}_4$ - FeN_x/C obtained from atomic resolution STEM-EDS imaging (E-G): Co Ka1 (E), Mn Ka1 (F), and Fe Ka1 (G).

The nano boundaries between these metal oxides and GNP are examined with TEM. Figure 2A-2C shows TEM images of $\text{Mn}_{1.5}\text{Co}_{1.5}\text{O}_4\text{-FeN}_x/\text{C}$. Some small darker and round regions are seen, and identified as $\text{Mn}_{1.5}\text{Co}_{1.5}\text{O}_4$ particles. The positions of GNP can also be recognized from the larger and lighter regions. However, the boundaries between $\text{Mn}_{1.5}\text{Co}_{1.5}\text{O}_4$ particles and GNP are unclear, which implies that the nano boundaries are well formed between the two materials with no gaps. Figure 2D shows TEM image of unsupported $\text{Mn}_{1.5}\text{Co}_{1.5}\text{O}_4$ with measured particle sizes around 10–20 nm, which is consistent with that of the XRD results. The purity and uniformity of $\text{Mn}_{1.5}\text{Co}_{1.5}\text{O}_4\text{-FeN}_x/\text{C}$ are examined by atomic resolution elemental mapping with STEM-EDS imaging. Figure 2E-2G shows elemental mapping of Co, Mn and Fe, respectively. The spatial distributions of Figure 2E and Figure 2F are matched very well, which indicates that the $\text{Mn}_{1.5}\text{Co}_{1.5}\text{O}_4$ is a uniform bimetal oxide, instead of a mixture of $\alpha\text{-Mn}_2\text{O}_3$ and Co_3O_4 . The crystals of $\text{Mn}_{1.5}\text{Co}_{1.5}\text{O}_4$, are formed when the Co atoms are replaced by some Mn atoms in the spinel structure of Co_3O_4 . The Fe element is evenly dispersed on the small graphene sheets. The spatial distribution of Fe element (see Figure 2G) is also approximately matched with that of $\text{Mn}_{1.5}\text{Co}_{1.5}\text{O}_4$, which indicates that the nano boundaries between FeN_x/C and $\text{Mn}_{1.5}\text{Co}_{1.5}\text{O}_4$ are well formed. The elemental content of $\text{Mn}_{1.5}\text{Co}_{1.5}\text{O}_4\text{-FeN}_x/\text{C}$ and $\text{Mn}_{1.5}\text{Co}_{1.5}\text{O}_4$ is measured with STEM-EDS, and listed in Table 1. Equal Mn and Co atomic concentrations of are seen, which matches the elemental composition of $\text{Mn}_{1.5}\text{Co}_{1.5}\text{O}_4$ and the XRD results.

Table 1. Relative metal contents in $\text{Mn}_{1.5}\text{Co}_{1.5}\text{O}_x\text{-FeN}_x/\text{C}$ and $\text{Mn}_{1.5}\text{Co}_{1.5}\text{O}_x$ samples obtained from STEM-EDS analysis (Note: The C% content is excluded for clarification).

Sample		Mn%	Co%	Fe%	O%	Total
MnCoO_x-FeN_x/C	w%	24.9	26.9	4.6	43.6	100
	a.t.%	12.2	12.3	2.2	73.3	100
MnCoO_x	w%	31.1	29.3	-	39.6	100
	a.t.%	14.9	15.1	-	70.0	100

3.3 Electrocatalytic Activity and Mechanisms of the ORR at the $\text{Mn}_{1.5}\text{Co}_{1.5}\text{O}_4\text{-FeN}_x/\text{C}$ Nanocomposite electrode. The electrochemical behaviors of various non-precious nanocomposites coated GC electrodes are initially examined by cyclic voltammetry (CV) in 0.1M KOH in the absence of oxygen, as shown in Figure 3A-B. An oxidation peak at ~1.0V and a reduction peak appearing between 0.5–0.7V are seen for the samples of $\text{Mn}_2\text{O}_3/\text{C}$, $\text{Mn}_{1.5}\text{Co}_{1.5}\text{O}_4/\text{C}$ and $\text{Mn}_{1.5}\text{Co}_{1.5}\text{O}_4\text{-FeN}_x/\text{C}$. It is noticeable that all of the three materials contain Mn element in their composition, indicating redox peaks for Mn ion oxidation and reduction. No peak is observed for the polarization curve obtained from the $\text{Co}_3\text{O}_4/\text{C}$ nanocomposite. In addition, no peak is observed for the FeN_x/C electrode, however, the background current increases when the potential is less than 0.8V. The rapid increase in background current at the lower potential is likely due to ions adsorption and desorption at the FeN_x/C surface. The ORR catalytic activity is detected by bubbling O_2 through the electrolyte solution. The catalytic activity is accurately analyzed by the rotating disk electrode method (RDE). Figure 3C shows polarization curves for the mono-metal oxides, and bimetal oxide coated RDEs in O_2 saturated 0.1M KOH. The ORR limiting current increases in the order of $\text{Mn}_{1.5}\text{Co}_{1.5}\text{O}_4/\text{C} > \text{Mn}_2\text{O}_3/\text{C} > \text{Co}_3\text{O}_4/\text{C}$. The half wave potential positively shifts from 0.73V for $\text{Mn}_2\text{O}_3/\text{C}$ to 0.76V for $\text{Mn}_{1.5}\text{Co}_{1.5}\text{O}_4/\text{C}$, which implies that the $\text{Mn}_{1.5}\text{Co}_{1.5}\text{O}_4/\text{C}$ has better catalytic activity than that of the mono-metal oxides $\text{Co}_3\text{O}_4/\text{C}$ and $\text{Mn}_2\text{O}_3/\text{C}$ investigated in this study. The enhancement of activity at the bimetal oxide is attributed to a synergistic effect of different metal atoms in the bimetal crystal. The Co_3O_4 shows

a spinel structure, with Co^{2+} ions in tetrahedral interstices and Co^{3+} ions in the octahedral interstices of the cubic close-packed lattice of oxide anions. The Mn is also able to form a Mn_3O_4 spinel structure. When Co and Mn form a bimetal oxide, the atoms of Co and Mn are positioned in the same spinel structure, which changes the parameters of their original structure, resulting in smaller crystallite size and particle size as shown by XRD and TEM results. The smaller crystal and particle size of a catalyst are corresponding to the higher surface area, the more active catalytic sites, and the higher catalytic activity for ORR. Therefore, we call this phenomenon as synergistic catalytic effect of bimetal composition. Figure 3D shows polarization curves of FeN_x/C , $\text{Mn}_{1.5}\text{Co}_{1.5}\text{O}_4/\text{C}$, and $\text{Mn}_{1.5}\text{Co}_{1.5}\text{O}_4\text{-FeN}_x/\text{C}$ coated RDEs in O_2 saturated 0.1 M KOH. The highest limiting current and the most positive half wave potential (0.82V) is observed for the $\text{Mn}_{1.5}\text{Co}_{1.5}\text{O}_4\text{-FeN}_x/\text{C}$ nanocomposite-coated RDE.

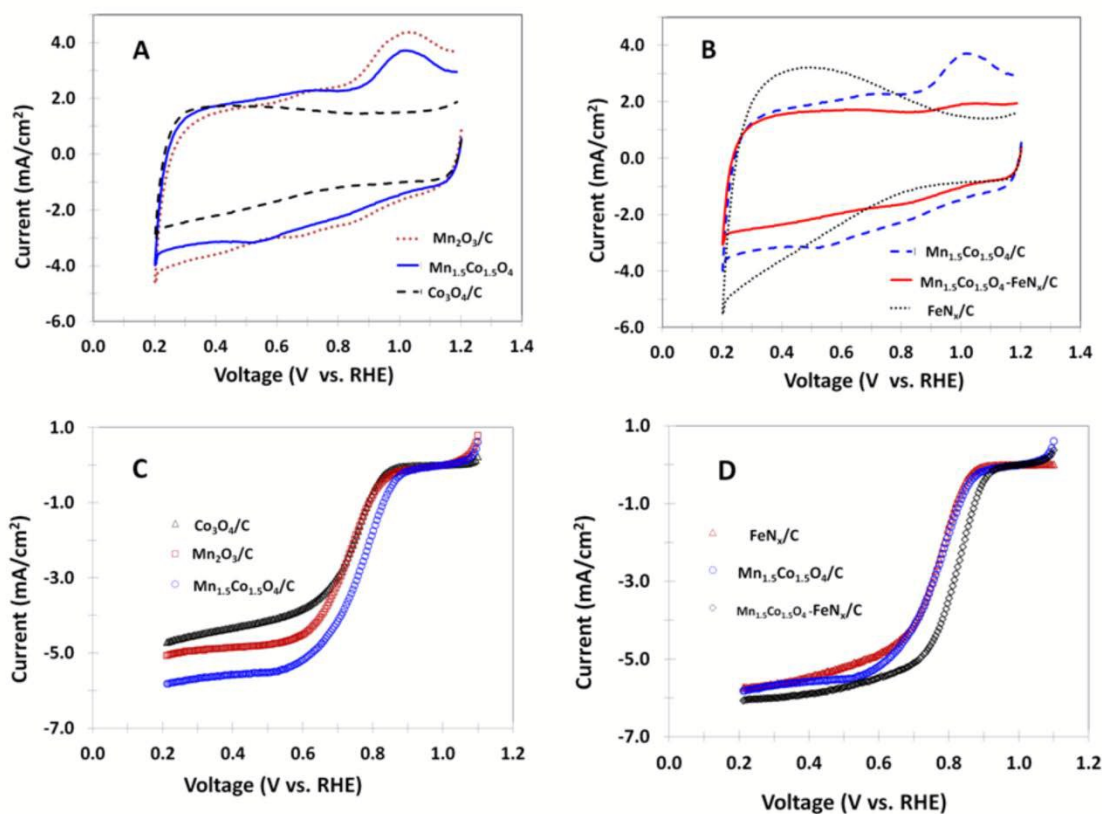


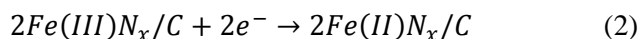
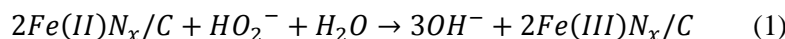
Fig. 3. Cyclic voltammograms of the different nanocomposites coated GC disk electrodes in argon saturated 0.1M KOH, 50 mV/s (A-B); and polarization curves of the same nanocomposites coated disk electrodes in O_2 saturated 0.1M KOH, 10 mV/s, rotation rate 1600 rpm (C-D).

Table 2. Electrochemical parameters of ORR at different nanocomposites coated electrodes in 0.1M KOH obtained from RDE and RRDE experiments.

Parameters	Co ₃ O ₄ /C	Mn ₂ O ₃ /C	Mn _{1.5} Co _{1.5} O ₄ /C	FeN _x /C	Mn _{1.5} Co _{1.5} O _x -FeN _x /C
E _{1/2} (V)	0.74	0.73	0.76	0.77	0.82
Tafel slope (mV/dec)	49	63	54	52	35
H ₂ O ₂ % yield at 0.6V	57.4	21.6	16.1	7.3	4.8
Electron transfer number at 0.6V	2.85	3.57	3.68	3.85	3.90

The enhancement of catalytic activity at the Mn_{1.5}Co_{1.5}O₄-FeN_x/C nanocomposite is attributed to a secondary synergistic effect of ORR at the nano boundaries, where the oxygen molecules are catalyzed by two types of catalytic sites, or the bimetal atoms, Mn-Co, at the Mn_{1.5}Co_{1.5}O₄ site, and the Fe atom at FeN_x/C site. The polarization curves of these catalysts coated RDEs are further analyzed with Tafel plots. The half wave potentials and Tafel slopes of ORR at these polarization curves are listed in Table 2. The Mn_{1.5}Co_{1.5}O₄-FeN_x/C nanocomposite has the smallest Tafel slope (35 mV/dec), which indicates an advantage of fast electron transfer between the oxygen molecules and the catalyst coated electrode. The number of electron transfer and the yield of intermediate product, H₂O₂, for ORR are obtained from the RRDE data. Figure 4A-B shows RRDE polarization curves of ORR at different nanocomposites coated GC disks and Pt-ring electrode in O₂ saturated 0.1M KOH. The current densities in Figure 4 are somewhat different from that in Figure 3. This difference often happens when the RDE and RRDE experiments are carried out with different electrodes that have different electrode areas. In the present research we used different electrodes for RDE (0.196 cm²) and RRDE (0.247 cm²) experiments, respectively. Due to the catalyst loading on the RDE and RRDE was exact the same (0.04 mg of metal oxide), which caused the catalyst dispersion and concentration differences (0.2 mg·cm⁻² for RDE and 0.16 mg·cm⁻² for RRDE), and the current density a slightly difference. Fortunately, these differences will not affect our comparison of the catalyst performance. The goal of the RDE experiment is used for comparison of the catalyst activity and stability; but the goal of the RRDE experiment is used to compare the H₂O₂ yielding during the process of ORR. The higher ring current indicates the more H₂O₂ generated for ORR at the disk electrode and collected at the ring electrode. The magnitude of ring current is Co₃O₄/C > Mn₂O₃/C > Mn_{1.5}Co_{1.5}O₄/C > FeN_x/C > Mn_{1.5}Co_{1.5}O₄-FeN_x/C. Plots of the number of electron transfer and the yield of H₂O₂% versus disk potential are shown in Figure 4C-D, respectively. The yield of H₂O₂ is potential dependent, and a peak yield appears at ~0.6V. The electron transfer number and H₂O₂% yield at 0.6V are also summarized in Table 2. The peak yield of H₂O₂% at the Mn_{1.5}Co_{1.5}O₄-FeN_x/C nanocomposite is less than 5%. The very small H₂O₂ production is probably because a small part of electrode is incompletely covered by the catalyst coating. Apparently, the Mn_{1.5}Co_{1.5}O₄-FeN_x/C nanocomposite mainly catalyzes 4-electron oxygen reduction. The mechanism of ORR at the nanocomposite Mn_{1.5}Co_{1.5}O₄-FeN_x/C has been explained with Scheme 3, where a nano boundary is composed of Mn_{1.5}Co_{1.5}O₄ and FeN_x/C. When an oxygen molecule is diffused into a nano boundary, it is catalyzed simultaneously by the bimetal site, Mn-Co, and the FeN_x site. If any intermediate product, H₂O₂, is generated at the Mn-Co surface, it will be continuously reduced at the FeN_x site. In addition, the FeN_x/C is not only able to catalyze 4-

electron O_2 reduction to water, but also it is able to catalyze 2-electron H_2O_2 reduction to water with excellent activity [8, 10, 20, 41-42]. The mechanism is shown below,



At the $Mn_{1.5}Co_{1.5}O_4$ - FeN_x/C nanocomposite coated electrode, many hetero nano boundaries are evenly dispersed, containing functional groups of $Mn_{1.5}Co_{1.5}O_4$ and FeN_x/C , which promote a coordinative catalysis, realizing 4-electron oxygen reduction.

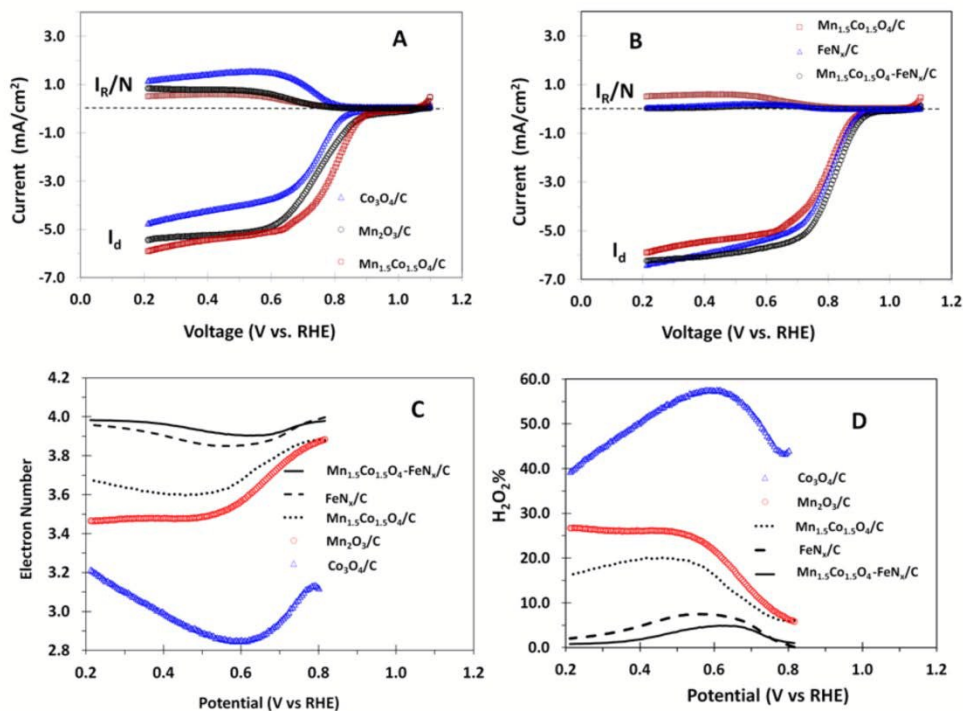


Fig.4. Polarization curves for the different nanocomposites coated GC disks and Pt-ring electrode in O_2 saturated 0.1M KOH (A-B). Note: The rotation rate is 1600 rpm, scan rate is 10 mV/s and the Pt-ring potential was held at 1.2V vs. RHE with a ring collection coefficient of 0.37. Plots of the number of electrons transferred per O_2 molecule (C), and the H_2O_2 % generation as a function of the disk potential (D).

3.4 Catalytic Kinetics of ORR at the $Mn_{1.5}Co_{1.5}O_4$ - FeN_x/C nano Composite. The catalytic kinetics of ORR at the $Mn_{1.5}Co_{1.5}O_4$ - FeN_x/C nanocomposite is investigated by analyzing the variations of the limiting current with rotation rate at the catalyst coated rotating disk electrode. Figure 5A shows polarization curves of $Mn_{1.5}Co_{1.5}O_4$ - FeN_x/C coated GC disk electrode in O_2 saturated 0.1M KOH at various rotation rates. The limiting current increases with increasing rotation rate. However, the limiting current is not proportional to the rotation rate at higher rotation rates, which gradually deviates from the values calculated by the Levich equation [7-8]. Figure 5B shows Levich plots at various electrode potentials. The dotted line is the calculated results for 4-electron oxygen reduction by diffusion controlled process. At higher potentials, there are more deviations from that of the calculated dotted line. Figure 5C shows Kotecky-Levich plots [7-8], all of

which are straight lines, and parallel to that of the calculated line (the dotted) for 4-electron oxygen reduction by diffusion controlled process, which indicates that the catalytic process belongs to a process of 4-electron oxygen reduction at the $\text{Mn}_{1.5}\text{Co}_{1.5}\text{O}_4\text{-FeN}_x/\text{C}$ nanocomposite coated electrode. The kinetic rate constants are calculated from the intercepts of the Koutecky-Levich plots, and listed in Table 3. At 0.7V, the kinetic rate constant is $7.6 \times 10^{-2} \text{ cm} \cdot \text{s}^{-1}$, which is higher than that of silver alloy nano particles ($6.8 \times 10^{-2} \text{ cm} \cdot \text{s}^{-1}$) [20] for catalytic ORR in alkaline media.

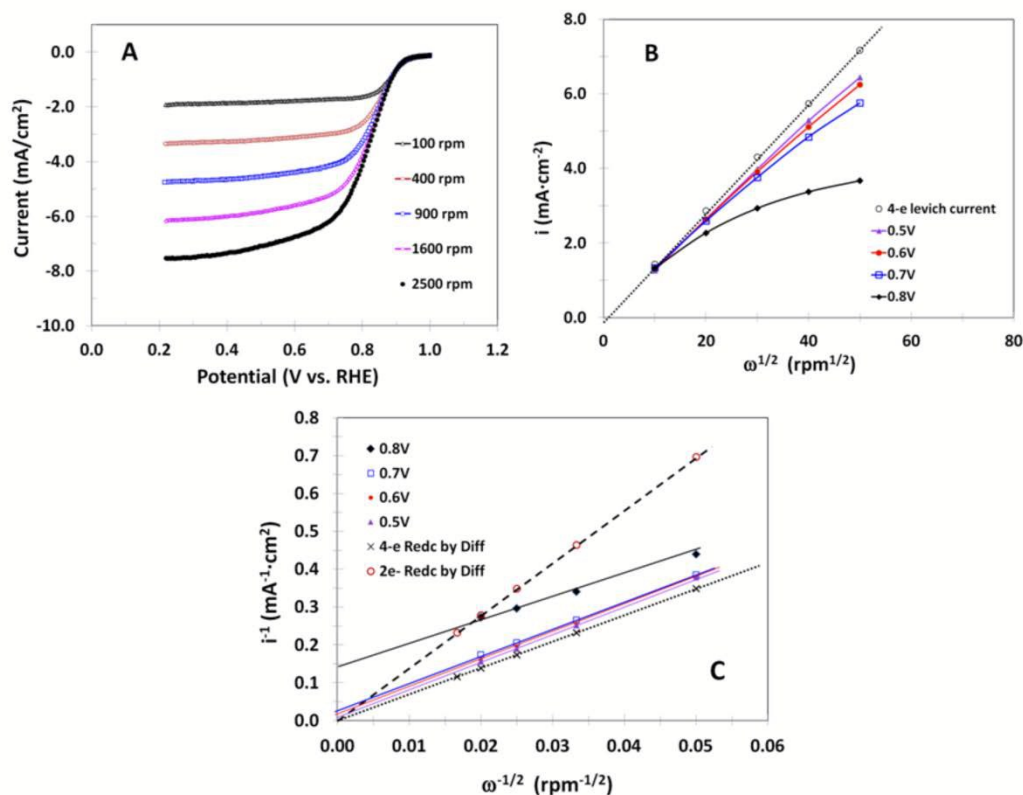


Fig. 5 (A) Polarization curves of $\text{Mn}_{1.5}\text{Co}_{1.5}\text{O}_4\text{-FeN}_x/\text{C}$ coated GC disk electrode in O_2 saturated 0.1M KOH at different rotation rates. Scan rate: 10 mV/s. (B) Levich plots of i versus $\omega^{1/2}$. (C) Koutecky-Levich plots of i^{-1} versus $\omega^{-1/2}$.

Table 3. Kinetic rates constant at $\text{Mn}_{1.5}\text{Co}_{1.5}\text{O}_x\text{-FeN}_x/\text{C}$ nanocomposite coated electrode in O_2 saturated 0.1M KOH.

Catalyst	Kinetic rate constant ($\text{cm} \cdot \text{s}^{-1}$)			
	0.8V	0.7V	0.6V	0.5V
$\text{Mn}_{1.5}\text{Co}_{1.5}\text{O}_4\text{-FeN}_x/\text{C}$	1.4×10^{-2}	7.6×10^{-2}	11.7×10^{-2}	24.9×10^{-2}

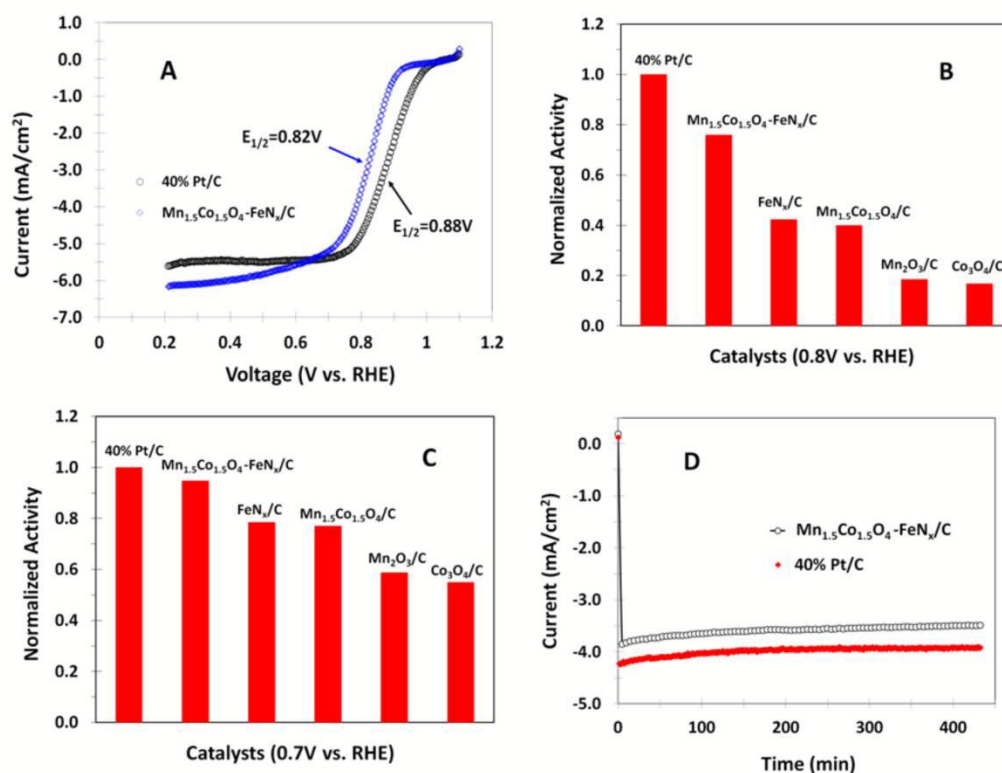


Fig. 6 Polarization curves for (A) Mn_{1.5}Co_{1.5}O₄-FeN_x/C and 40% Pt/C coated GC disk electrodes in O₂ saturated 0.1M KOH with a scan rate of 10 mV/s and rotation rate of 1600 rpm. (B-C) Normalized activities at 0.8 and 0.7V, respectively, where the ORR activity of 40% Pt/C is set equal to 1. (D) Chronoamperometric curves at 0.7V for Mn_{1.5}Co_{1.5}O₄-FeN_x/C and 40% Pt/C coated GC electrode in O₂ saturated 0.1M KOH with a rotation rate of 900 rpm.

3.5 Comparison with Pt Catalyst. The activity and stability of Mn_{1.5}Co_{1.5}O₄-FeN_x/C nanocomposite are compared with commercially available Pt catalyst containing 40% Pt and 60% active carbon (40% Pt/C). The catalyst loadings on the electrode were 0.2 mg·cm⁻² on the electrode for the metal oxide and 40% Pt/C samples, respectively. 5% Nafion was added as a binder in all catalyst coatings. Figure 6A shows polarization curves of Mn_{1.5}Co_{1.5}O₄-FeN_x/C and 40% Pt/C coated rotating GC disk electrodes in O₂ saturated 0.1M KOH, respectively. There is 60 mV half wave potential difference between Mn_{1.5}Co_{1.5}O₄-FeN_x/C and 40% Pt/C. The catalytic activities are compared, as shown in Figure 6B-C by assuming the activity of 40% Pt/C equal to 1. At 0.7V the activity of Mn_{1.5}Co_{1.5}O₄-FeN_x/C reaches 95% that of the 40% Pt/C. The catalytic stability was also examined by chronoamperometric experiment at 0.7V and 900 rpm rotation rate, during which oxygen gas was bubbled through the electrolyte continuously. Figure 6D shows chronoamperometric curves of Mn_{1.5}Co_{1.5}O₄-FeN_x/C and 40% Pt/C coated GC disk electrodes in 0.1M KOH solution, respectively. The approximately paralleled curves obtained indicates that the catalytic stability of the Mn_{1.5}Co_{1.5}O₄-FeN_x/C is comparable to that of the 40% Pt/C.

4.0 CONCLUSION

In this study we demonstrated a method of making non-precious metal oxide nanocomposite catalysts and achieved double synergistic effects for catalytic oxygen reduction. A precious mono-metal oxide's catalytic activity can be enhanced by incorporating a second non-precious metal element into its crystal structure to generate a nano crystal material with uniform elemental spatial distribution. The addition of the second metal in the crystal structure of a mono-metal oxide results in smaller crystallite size, particle size, and higher active surface area for the bimetal oxide, leading to higher catalytic activity. The catalytic activity of the bimetal oxide can be further enhanced by supporting it on a functional carbon material containing FeN_x functional groups. The bimetal oxide, the functional carbon and the electrolyte form nano boundaries, which are the active sites for catalytic oxygen reduction. The FeN_x group is functioned as a mediator to remove H₂O₂ intermediate generated in the catalytic process of oxygen reduction, and promoting oxygen to be catalyzed through a complete 4-electron reduction. Our work provides a new pathway in design and synthesis of novel non-precious nanocomposite catalysts.

ACKNOWLEDGMENT

The authors would like to thank Dr. Wen-An Chiou and Dr. Sz-Chian Liou at University of Maryland for assisting TEM and STEM analyses. Thanks to the U.S. Department of the Army and U.S. Army Materiel Command for supporting this work.

REFERENCES

1. J. Marcinkoski, B. D. James, J. A. Kalinoski, W. Podolski, T. Benjamin, and J. Kopasz, *J. Power Sources*, 2011, 196, 5282–5292.
2. J. P. Collman, M. Marrocco, P. Denisevich, C. Koval, and F. C. Anson, *J. Electroanal. Chem.*, 1979, 101 (1), 117.
3. J. P. Collman, P. Denisevich, Y. Konai, M. Marrocco, C. Koval, and F. C. Anson, *J. Am. Chem. Soc.*, 1980, 102 (19), 6027-6036.
4. X. M. Hu, D. G. Xia, L. Zhang, and J. J. Zhang, *J. Power Sources*, 2013, 231, 91-96.
5. H. D. Sha, X. X. Yuan, L. Li, Z. Ma, Z. F. Ma, L. Zhang, and J. J. Zhang, *J. Power Sources*, 2014, 255, 76-84.
6. R. Z. Jiang, D. T. Tran, J. McClure, and D. Chu, *Electrochem. Commun.*, 2012, 19, 73–76.
7. R. Z. Jiang, D. T. Tran, J. McClure, and D. Chu, *Electrochim. Acta*, 2012, 75, 185–190.
8. R. Z. Jiang, and D. Chu, *J. Power Sources*, 2014, 245, 352–361.
9. D. Chu, and R. Z. Jiang, *Solid State Ionics*, 2002, 148, 591-599.
10. R. Z. Jiang, and D. Chu, *J. Electrochem. Soc.*, 2000, 147 (12), 4605-4609.
11. G. Wu, K. L. More, C. M. Johnston, and P. Zelenay, *Science*, 2011, 332, 443-447.
12. D. H. Li, C. X. Ly, L. Liu, Y. Z. Xia, X. L. She, S. J. Guo, and D. J. Yang, *ACS Cent. Sci.*, 2015, 1, 261–269.
13. J. P. McClure, R. Z. Jiang, D. Chu, and P. S. Fedkiw, *Carbon*, 2014, 79, 457-469.
14. D. G. Guo, R. Shibuya, C. Akiba, S. Saji, T. Kondo, and J. Nakamura, *Science*, 2016, 351 (6271), 361-365.
15. J. P. McClure, C. K. Devine, R. Z. Jiang, D. Chu, J. J. Cuomo, G. N. Parsons, and P. S. Fedkiw, *J. Electrochem. Soc.*, 2013, 160, F769-F778.
16. J. Zhang, S. Wu, X. Chen, M. Pan, and S. C. Mu, *J. Power Sources*, 2014, 271, 522.
17. H. Yin, C. Z. Zhang, F. Liu, and Y. L. Hou, *Adv. Funct. Mater.*, 2014, 24, 2930–2937.
18. J. P. McClure, J. D. Thornton, Z. Jiang, D. Chu, J. J. Cuomo, and P. S. Fedkiw, *J. Electrochem. Soc.*, 2012, 159, F733-F742.
19. K. P. Gong, F. Du, Z. H. Xia, M. Durstock, L. M. Dai, *Science* 2009, 323, 760-764.
20. R. Z. Jiang, D. T. Tran, J. McClure, and D. Chu, *ACS Appl. Mater. Interfaces*, 2015, 7, 18530–18539.

21. Y. Y. Ma, R. F. Wang, H. Wang, J. L. Key, and S. Ji, *J. Power Sources*, 2015, 280, 526-532.
22. N. I. Andersen, A. Serov, and P. Atanassov, *Appl. Catal., B* 2015, 163 623–627.
23. H. Y. Park, T. J. Shin, H. I. Joh, J. H. Jang, D. Ahn, and S. J. Yoo, *Electrochem. Commun.*, 2014, 41, 35–38.
24. T. R. Zhang, F. Y. Cheng, J. Y. X. Hu, and J. Chen, *Adv. Energy Mater.*, 2015, 5, 1400654.
25. D. J. Davis, T. N. Lambert, J. A. Vigil, M. A. Rodriguez, M. T. Brumbach, E. N. Coker, and S. J. Limmer, *J. Phys. Chem. C*, 2014, 118, 17342–17350.
26. C. Shia, G. L. Zang, Z. Zhang, G. P. Sheng, Y. X. Huang, G. X. Zhao, X. K. Wang, and H. Q. Yu, *Electrochim. Acta*, 2014, 132, 239–243.
27. F. Y. Cheng, Y. Su, J. Liang, Z. L. Tao, and J. Chen, *Chem. Mater.*, 2010, 22, 898–905.
28. Y. G. Wang, L. Cheng, F. Li, H. M. Xiong, and Y. Y. Xia, *Chem. Mater.*, 2007, 19, 2095-2101.
29. J. B. Xu, P. Gao, and T. S. Zhao, *Energy Environ. Sci.*, 2012, 5, 5333–5339.
30. Y. Y. Liang, Y. G. Li, H. J. Wang, J. G. Zhou, J. Wang, T. Regier, and H. J. Dai, *Nat. Mater.*, 2011, 10, 780-786.
31. S. Bag, K. Roy, C. S. Gopinath, and C. R. Raj, *ACS Appl. Mater. Interfaces*, 2014, 6, 2692–2699.
32. H. Q. Dong, Y. Y. Chen, M. Han, S. L. Li, J. Zhang, J. S. Li, Y. Q. Lan, Z. H. Dai and J. C. Bao, *J. Mater. Chem. A*, 2014, 2, 1272–1276.
33. T. Odedairo, X. C. Yan, J. Ma, Y. L. Jiao, X. D. Yao, A. J. Du, and Z. H. Zhu, *ACS Appl. Mater. Interfaces*, 2015, 7, 21373–21380.
34. S. Y. Liu, L. J. Li, H. S. Ahn, and A. Manthiram, *J. Mater. Chem. A*, 2015, 3, 11615–11623.
35. Y. T. Luo, J. H.; Guo, Y. H. Liu, Q. Shao, C. S. Wang, and D. Chu, *J. Membr. Sci.*, 2012, 423, 209–214.
36. Y. T. Luo, J. H. Guo, C. S. Wang, and D. Chu, *Electrochem. Commun.* 2012, 16, 65-68.
37. Y. S. Li, T. S. Zhao, and X. X. Liang, *J. Power Sources*, 2009, 187, 387-392.
38. E. E. Switzer, T. S. Olson, A. K. Datye, P. Atanassov, M R. Hibbs, C. Fujimoto, and C. Cornelius, *Electrochim. Acta*, 2010, 55, 3404-3408.
39. B. Y. Xia, Y. Yan, N. Li, H. B. Wu, X. W. Lou and X. Wang, *Nature Energy*, 2016, 1, 15006.
40. U. I. Kramm, I. Abs-Wurmbach, I. Herrmann-Geppert, J. Radnik, S. Fiechter, and P. Bogdanoff, *J. Electrochem. Soc.* 2011, 1, 158, B69-B78.
41. Q. Wu, M. Nelson, S. Ma, H. Meng, G. F. Cui, and P. K. Shen, *Carbon*, 2011, 49, 3972-3982.
42. S. Li, L. Zhang, J. Kim, M. Pan, Z. Shi, and J. J. Zhang, *J. J. Electrochim. Acta*, 2010, 55, 7346–7353.

Graphical Abstracts

A nanocomposite material containing non-precious bimetal oxides and FeN-doped carbon was synthesized with double synergistic effect for ORR.

